Post-Leaching Water, Ultrasonic and Mild-Acid Washing for Purifying Graphite Recovered from Spent NMC111 Lithium-Ion Batteries

batteries

MDPI

Article

Post-Leaching Water, Ultrasonic and Mild-Acid Washing for Purifying Graphite Recovered from Spent NMC111 Lithium-Ion Batteries

José E. Arevalo-Fester [1,*], Magnus Larsson [2], Sofia Öiseth [3], Jonas Löfvendahl [3], Mykhailo Zhybak [4], Erik Khranovskyy [4] and Martina Petranikova [1]

[1] Nuclear Chemistry and Industrial Materials Recycling, Department of Chemistry and Chemical Engineering, Chalmers University of Technology, SE-412 96 Gothenburg, Sweden; martina.petranikova@chalmers.se
[2] 2D fab AB, Montörvägen 7, SE-853 50 Sundsvall, Sweden; magnus.larsson@2dfab.se
[3] Chalmers Industriteknik, Sven Hultins Plats 1, SE-412 58 Gothenburg, Sweden; sofia.oiseth@chalmersindustriteknik.se (S.Ö.); jonas.lofvendahl@chalmersindustriteknik.se (J.L.)
[4] GRAFREN, Industrigatan 9Q, SE-582 77 Linköping, Sweden; cto@grafren.se (M.Z.); ceo@grafren.se (E.K.)
* Correspondence: jose.arevalo@chalmers.se

Abstract

Recovered graphite from spent lithium-ion batteries is an important secondary resource that can reduce reliance on primary graphite and lower the environmental footprint of battery production. In this work, graphite obtained as a carbon-rich residue after industrial hydrometallurgical leaching of NMC111 black mass (2 M H_2SO_4 + 3% H_2O_2) is subjected to three post-leaching washing treatments to assess how far simple, low-intensity steps can further clean the leach residue while preserving the carbon structure. The washing routes are water washing (GW), water washing with ultrasonication (GU) and mild sulfuric-acid washing with 0.1 M H_2SO_4 (GA). ICP-OES and SEM–EDX show that, relative to the leached black mass, all washing treatments reduce residual transition-metal contents by two to three orders of magnitude, and that the mild acid wash provides the lowest bulk metal levels, with several elements at or below detection limits. X-ray diffraction and Raman spectroscopy indicate graphite-dominated patterns and improved structural order, with the ID/IG ratio decreasing from 0.62 (GW) to 0.11 (GA) and the corresponding in-plane crystallite size increasing from 30.6 nm to 168 nm. Overall, the mild acid washing step is the most effective low-impact post-leaching purification route, yielding a thoroughly cleaned low-metal graphite fraction that preserves the graphite framework and constitutes a suitable intermediate for further upgrading or reuse in secondary applications.

Keywords: lithium-ion batteries; recovered graphite; black mass; washing treatments; mild acid purification; structural characterization

Academic Editor: Xizhang Wang

Received: 28 April 2026
Revised: 1 June 2026
Accepted: 2 June 2026
Published: 5 June 2026

1. Introduction

The rapid deployment of electric vehicles and stationary energy storage has made lithium-ion batteries (LIBs) a strategically important technology for decarbonization [1]. LIB manufacturing exceeded 1 TWh yr^{-1} in 2024, with automotive applications representing more than 80% of installed capacity. This growth intensifies two interlinked challenges: securing sustainable supplies of critical raw materials such as Li, Co, Ni, Mn, Cu, and graphite, and mitigating the environmental and social impacts associated with mining,

refining and end-of-life management of LIBs [2,3]. These concerns are driving the development of closed-loop recycling schemes that recover and requalify all functional components of spent batteries for reintegration into new cells [4–7].

Graphite accounts for roughly 12–21 wt% of a typical EV battery pack and is the single most abundant active material by mass [8–10]. Its supply chain is exposed to both geopolitical and environmental risks: natural graphite production is geographically concentrated, with China dominating global output and a few countries such as Mozambique, Madagascar and Brazil providing most of the remaining supply, while synthetic graphite relies on energy-intensive graphitization of petroleum coke at temperatures near 3000 °C, with a correspondingly high CO_2 footprint [11,12]. With global graphite demand projected to reach several million tons per year by 2035, primary production alone is unlikely to meet future anode requirements without substantial environmental cost [13,14]. In this context, recovering and reusing anode graphite from spent LIBs offers an important opportunity to improve resource security, reduce energy use and greenhouse gas emissions, and embed circularity in battery value chains [15].

Compared with cathode metal recovery, however, graphite recycling is still underdeveloped. Its relatively low market price, the complexity of removing the solid–electrolyte interphase (SEI), binders and electrolytes, and the stringent specifications for battery grade material (high purity, high crystallinity, high initial Coulombic efficiency (ICE)) have limited industrial implementation [15,16]. Recent studies have demonstrated that spent graphite can be regenerated or upgraded via thermal regraphitization, chemical purification, surface modification and upcycling into higher value products such as graphene, aerogels or activated carbons, often achieving electrochemical performance comparable to or better than commercial anodes and substantially lower life cycle impacts [17–20]. Nonetheless, meeting battery grade quality typically requires very low levels of metallic and inorganic impurities, controlled surface chemistry and standardized testing protocols, which remain challenging for heterogeneous industrial black mass [21–25].

Graphite purification methods can be broadly grouped into physical, chemical, and combined approaches that aim to remove impurities while preserving the underlying carbon framework. Acid-based hydrometallurgical treatments are among the most established routes, using mineral or organic acids (e.g., H_2SO_4, HCl, oxalic or citric acid) to selectively dissolve transition metal residues such as Ni, Co, Mn and Cu. Dilute sulfuric acid, often aided by oxidants like H_2O_2, can achieve high leaching efficiency with limited damage to the graphite structure, whereas organic acids such as oxalic acid offer potentially lower environmental burdens [13,26]. Thermal purification, typically between about 700 and 3000 °C under inert or reducing atmospheres, is effective for decomposing PVDF, removing organic species and, at very high temperatures, regraphitizing disordered carbon, but it is energy intensive and associated with significant CO_2 emissions More recently, solvent-based strategies including supercritical CO_2, co-solvents and deep eutectic solvents have been explored for binder and electrolyte removal without strong mineral acids, and electrochemical techniques such as anodic oxidation and electro dissolution have been proposed to dissolve metallic and fluorinated species at lower specific energy input [15,26–28]. Hybrid flowsheets combining flotation, selective leaching and moderate thermal or solvent steps have achieved substantial reductions in ash and metal content, but often still fall short of full battery grade specifications and may involve complex process integration [24].

Despite this progress, several hurdles continue to limit the large-scale recycling of anode graphite from spent LIBs. PVDF binder and separator fragments are chemically robust, frequently requiring sequential or combined treatments for effective removal. Achieving low transition-metal contents without degrading graphite crystallinity or introducing new contaminants remains challenging. In addition, the generation of acidic waste streams,

the energy demand of high-temperature treatments and the recovery and reuse of organic solvents are critical constraints for the environmental and economic viability of current approaches. Recent research has therefore shifted towards "milder" process conditions that combine dilute leaching agents, mechanical or ultrasonic agitation and targeted binder-removal steps, while being evaluated within life-cycle and techno-economic frameworks [11,26,29].

At the same time, battery-grade graphite and other electrode materials are expected to meet very stringent impurity thresholds, with transition-metal contaminants typically controlled to the low-ppm range to avoid adverse effects on cell performance and lifetime [30]. Meeting such low impurity levels is particularly challenging for graphite recovered from industrial black mass and generally necessitates a combination of chemical and thermal purification steps.

In this context, the present study investigates the recovery and cleaning of graphite from industrial black mass derived from spent NMC111 lithium-ion batteries. The as-received black mass is a complex mixture containing transition metals, conductive additives, polymers, electrolytes, binders and carbonaceous phases. After hydrometallurgical leaching of valuable metals, we systematically compare three post-leaching washing strategies: water washing, ultrasonic-assisted washing and diluted sulfuric acid washing, designed to reduce residual metallic and inorganic impurities while preserving the structural and thermal integrity of the recovered graphite. Using complementary characterization methods (SEM–EDX, ICP OES, TGA/DSC, XRD and Raman spectroscopy), we evaluate how far such mild treatments can clean and restore graphite obtained from real industrial black mass. The resulting material is discussed as a thoroughly cleaned intermediate that requires further purification or regeneration steps before reaching battery-grade quality, or that can be directly used in secondary applications such as conductive composites, lubricants, activated carbons or anodes for less demanding electrochemical systems [31].

In the present industrial flow, the initial 2 M H_2SO_4 + 3% H_2O_2 leaching step is optimized for dissolving cathode metals and recovering them from solution, not for producing a clean graphite product. After leaching and neutral rinsing, the solid residue still contains surface-bound metal species, fine oxide or spinel fragments and fluorinated binder/separator debris attached to the graphite grains. The post-leaching washing steps investigated here are therefore designed to target these residual surface and particulate impurities under much milder conditions, while preserving the graphite framework.

2. Materials and Methods

The black mass was obtained from battery packs supplied by Volvo Cars AB. Volvo Cars AB and Stena Recycling AB, in Gothenburg, Sweden conducted the discharge and disassembly. The material then underwent mechanical treatment and separation by Akkuser Oy, Nivala, Finland.

Before leaching, the as-received black mass from NMC111 lithium-ion batteries was sieved by the Industrial Materials Recycling group at Chalmers University of Technology (Sweden) to a particle size below 150 µm, yielding a concentrated and relatively uniform powder consisting of graphite anode material, cathodic NMC111 particles, plastic separator fragments, and aluminum and copper current collector foils. The leaching process was performed using 2 M sulfuric acid (Sigma-Aldrich (Merck KGaA), Darmstadt, Germany) and 3% hydrogen peroxide (Nouryon AB, Gothenburg, Sweden) at 60 °C for 2 h, maintaining a solid-to-liquid ratio of 1:20 and continuous agitation at 300 RPM. After leaching, the slurry was filtered and rinsed with deionized water until the pH reached 7, then dried overnight at 60 °C [23]. The leached black mass was then divided into three equal portions for further processing.

Three different washing methods were employed to eliminate residual metal contaminants from the black mass following the leaching process. For each method, 10 g portions of dried leached black mass were placed into separate 500 mL beakers. In the first treatment (GW), 300 mL of deionized water was added, and the suspension was stirred at room temperature at 300 rpm for 2 h. After completion, the sample was filtered and rinsed twice with 250 mL of deionized water. The second treatment (GU) followed the same procedure as GW but included ultrasonic treatment using a sonicator probe (Infitek USCG300N, Infitek, Shanghai, China, 24 kHz, nominal power 300 W), with pulses of 20 s on and 20 s off at 80% amplitude, applied in 5 min cycles every 60 min. After the ultrasonic treatment, the sample was similarly filtered and rinsed twice with 250 mL of deionized water. In the third washing method (GA), 300 mL of 0.1 M sulfuric acid (H_2SO_4) solution was added to the graphite and stirred at room temperature for 3 h. This sample was subsequently filtered and rinsed with 300 mL of deionized water. All washed samples were dried overnight at 60 °C before further analysis. The illustration of the preparation steps for the leaching of industrial black mass to enable graphite recovery is shown in Figure 1.

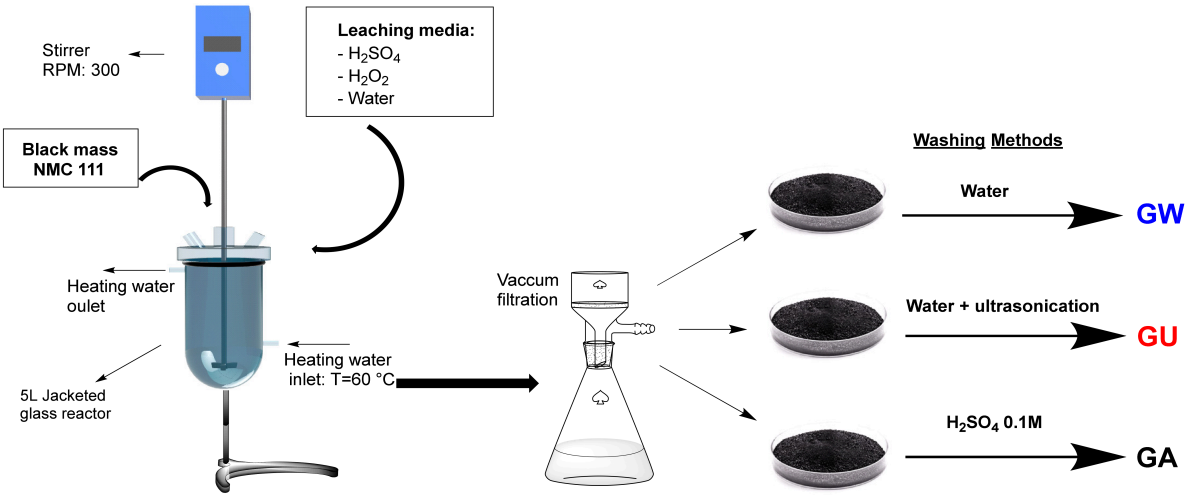

Figure 1. Process flow diagram showing the preparation steps for leaching NMC111 black mass to recover graphite.

Characterization of Carbon Materials

A comprehensive suite of advanced characterization techniques was employed to analyze the properties of recovered carbon materials. Among these, the metallic content was quantified using Inductively Coupled Plasma Optical Emission Spectroscopy (ICP-OES). For this purpose, samples were digested using 30 mL of aqua regia, prepared by mixing hydrochloric acid (HCl, 37%) and nitric acid (HNO_3, 65–67%) in a 3:1 volumetric ratio (*v*/*v*). Specifically, 0.25 g of dried solid powder was introduced into the acid mixture and reacted for 6 h at 80 °C under magnetic agitation at 300 rpm. The resulting solution was filtered, cooled to room temperature, and then diluted with 0.1 M HNO_3 before ICP-OES analysis. Measurements were conducted using a Thermo-Fisher Scientific iCAP™ 6000 Series spectrometer, Thermo Fisher Scientific, Waltham, MA, USA, providing accurate determination of trace metals in the graphite samples. For each sample, three independently digested replicates were measured by ICP-OES, and the concentrations reported in Table 1 represent the mean values, with the standard deviations reflecting the variability between these replicates.

Table 1. ICP–OES elemental concentrations in black mass (BM) and washed graphite fractions (mg g^{-1}). Standard deviations (SD) are shown in parentheses. For each washed sample, the row "removal vs BM (%)" reports the percentage decrease in concentration relative to BM for the corresponding element.

Samples	P	Ni	Co	Mn	Fe	Cu	Al	Li
BM	1.03 (0.04)	47.1 (0.6)	69.2 (0.8)	41.9 (0.6)	0.86 (0.07)	4.73 (0.16)	2.98 (0.11)	38.8 (0.5)
GW	0.075 (0.008)	0.062 (0.003)	1.054 (0.050)	0.017 (0.004)	0.178 (0.019)	0.082 (0.001)	0.013 (0.005)	0.297 (0.068)
GW removal vs. BM (%)	92.7	99.9	98.5	99.9	79.4	98.3	99.6	99.2
GU	0.058 (0.004)	0.060 (0.004)	1.061 (0.013)	0.020 (0.007)	0.172 (0.018)	0.083 (0.005)	0.010 (0.017)	0.44 (0.13)
GU removal vs. BM (%)	94.3	99.9	98.5	99.9	80.1	98.2	99.7	99.9
GA	0.056 (0.005)	0.037 (0.004)	0.466 (0.015)	ND	0.144 (0.008)	0.019 (0.012)	ND	0.175 (0.046)
GA removal vs. BM (%)	94.5	99.9	99.3	>99.9	83.3	99.6	>99.9	99.5

ND: not detected (below ICP-OES detection limit). Removal efficiencies were calculated as $(1 - C_{sample}/C_{BM}) \times 100$ using BM concentrations as reference; ">99.9" indicates that the element was not detected in the washed fraction, implying essentially complete removal.

X-ray diffraction (XRD) analysis was conducted to investigate the crystalline structure and degree of graphitization of the graphite-containing samples. Patterns were recorded using a powder diffractometer (XRPD, Bruker D8, Bruker, Billerica, MA, USA) with a Cu (λ = 1.54184 Å) radiation source, in a 2θ range of 10–80° and a rotational speed of 15 rpm. The operating current and voltage were 40 mA and 40 kV. The diffraction data provided information on the characteristic hexagonal crystal structure of graphite, especially the (002) basal plane reflection, which is indicative of interlayer spacing. Peak positions and shifts, intensities and peak widths were used to evaluate defects, strain and structural changes induced by the sample preparation and washing procedures. The measurements also enabled detection of metals or secondary phases in the black mass and washed fractions, providing insight into graphite purity and the effectiveness of the purification steps.

Thermogravimetric analysis (TGA) was carried out on a METTLER-TOLEDO TGA/DSC 3+ instrument, Mettler-Toledo, Columbus, OH, USA to evaluate the thermal stability and oxidation behavior of the graphite samples over a wide temperature range. The samples were heated from 30 °C to 800 °C at 10 °C min^{-1} under flowing synthetic air (oxidative atmosphere). Differential scanning calorimetry (DSC) was performed separately on a METTLER-TOLEDO DSC 5+, Mettler-Toledo, Columbus, OH, USA instrument under nitrogen, from 30 °C to 600 °C at the same heating rate, to detect endothermic and exothermic events associated with solvent/binder removal and possible phase transitions.

Field emission scanning electron microscopy (FESEM) was carried out using an FEI ESEM Quanta 200 microscope, FEI Company, Hillsboro, OR, USA, equipped with energy-dispersive X-ray spectroscopy (EDX) to analyze the morphology and microstructural features of the black mass and washed graphite-rich fractions, and to determine the elemental composition of these graphite-containing samples. Imaging was performed in low-vacuum mode at a pressure of 20 Pa. The electron beam was set at an acceleration voltage of 8–20 kV. The EDS system provided qualitative and semi-quantitative elemental analysis, enabling identification of residual metallic impurities and their distribution on the graphite surfaces. For each sample (BM, GW, GU and GA), EDX spectra were collected on multiple carbon-rich particles; in total, 10 individual particle regions were quantified per sample. The values reported in Table 2 correspond to the mean and one standard deviation over

these measurements. This combined approach allowed detailed study of morphological changes along with a clear insight into the effectiveness of the purification treatments.

Table 2. SEM–EDX surface elemental composition of BM, GW, GU and GA (wt%, mean ± SD).

Samples	P	Ni	Co	Mn	Al	C	O	F
BM	0.3 ± 0.1	7.4 ± 2	9.7 ± 1	6.5 ± 1	0.6 ± 0.2	48.9 ± 5	19.7 ± 3	6.28 ± 0.02
GW	0.04 ± 0.01 [1]	0.09 ± 0.01 [1]	0.23 ± 0.02	0.02 ± 0.01 [1]	0.2 ± 0.1	82.0 ± 0.9	5.2 ± 0.7	12.3 ± 0.5
GU	0.03 ± 0.01 [1]	0.07 ± 0.06 [1]	0.19 ± 0.04	0.02 ± 0.01 [1]	0.16 ± 0.05	82.1 ± 1.4	5.4 ± 0.4	12.0 ± 1.2
GA	0.02 ± 0.01 [1]	0.01 ± 0.01 [1]	0.07 ± 0.03 [1]	0.01 ±0.01 [1]	0.14 ± 0.04	81.9 ± 0.8	5.6 ± 0.5	12.2 ± 0.9

[1] Values below ~0.1 wt% are near or below the practical detection limit of SEM–EDX under the present conditions and should be interpreted as trace levels rather than precise concentrations. SEM–EDX is a semi-quantitative surface technique, and the reported values represent approximate surface compositions.

Raman spectroscopy was performed using a WITec Alpha300 R confocal Raman microscope, WITec GmbH, Ulm, Germany, equipped with a 532 nm laser. Raman spectra were acquired to assess structural order and defect density based on the characteristic D and G bands, their shifts and intensity variations, providing insights into strain, doping and chemical modifications of the graphite induced by processing. The I_D/I_G ratios were determined from the integrated peak areas of the D and G bands obtained by peak fitting, rather than from peak heights. Because the washed fractions still contained some non-graphitic components, such as fibrous separator and binder residues, as evidenced by SEM, spectra were acquired on regions where the characteristic graphite bands were clearly visible. For each sample (GW, GU and GA), 7 spectra were collected on visually identified graphite-rich areas distributed over different particles. The I_D/I_G ratios and the corresponding in-plane crystallite sizes La reported in Table 3 were obtained from these graphite-rich spectra and are used to describe the relative evolution of structural order across the washing sequence.

Table 3. Raman parameters for GW, GU, and GA.

Sample	D (cm^{-1})	G (cm^{-1})	G′ (cm^{-1})	I_D/I_G	La (nm)
GW	1351	1580	2752	0.62	30.6
GU	1349	1572	2700	0.52	36.6
GA	1345	1572	2696	0.11	168.4

3. Results

3.1. Efficiency of Washing Methods

The efficiency of the three washing routes was quantified by tracking changes in metallic impurity levels in the leach residue and washed fractions using inductively coupled plasma optical emission spectroscopy (ICP-OES). The analyzed elements (P, Ni, Co, Mn, Fe, Cu, Al and Li) represent the main cathode and collector-derived contaminants remaining in the graphite-rich solid after leaching. Their concentrations and standard deviations are summarized in Table 1 for the black mass (BM) and the three washed fractions (GW, GU and GA), providing a quantitative basis for comparing how each post-leaching treatment affects the composition of the graphite-rich solid.

The unprocessed black mass (BM) exhibited high concentrations of transition metals characteristic of the NMC111 cathode composition, along with lithium and minor metals derived from the current collectors and conductive additives. In Table 1, nickel and cobalt were quantified at 47.1 mg g^{-1} and 69.2 mg g^{-1}, respectively, while manganese reached 41.9 mg g^{-1} and lithium 38.8 mg g^{-1}. Aluminum (3.0 mg g^{-1}), iron (0.86 mg g^{-1}), and copper (4.73 mg g^{-1}) were also detected, reflecting residual contributions from aluminum

and copper foils [32], and phosphorus (1.03 mg g^{-1}), consistent with phosphate-based electrolyte additives, was also detected. The relatively small SD values for the major elements indicate consistent measurements and confirm the homogeneity of the black mass, providing a reliable baseline for evaluating the washing treatments.

3.1.1. Graphite Washed with Deionized Water (GW)

Washing the recovered graphite with deionized water caused a pronounced reduction in all metallic impurities, with most concentrations decreasing by approximately two to three orders of magnitude relative to the black mass. As shown in Table 1, nickel decreased from 47.1 mg g^{-1} to 0.062 mg g^{-1}, manganese from 41.9 mg g^{-1} to 0.017 mg g^{-1}, and cobalt from 69.2 mg g^{-1} to 1.05 mg g^{-1}. Lithium was reduced from 38.8 mg g^{-1} to 0.30 mg g^{-1}. Iron, copper, aluminum and phosphorus also decreased substantially, reaching 0.178 mg g^{-1}, 0.082 mg g^{-1}, 0.013 mg g^{-1} and 0.075 mg g^{-1}, respectively. In terms of removal efficiencies, this corresponds to ≈99–100% removal of Ni, Mn, Al and Li and ≈98–99% removal of Co and Cu relative to BM (Table 1). These results show that water washing effectively removes soluble salts and loosely bound metal-containing species, although measurable amounts of cobalt, lithium and other metals remain associated with the graphite.

3.1.2. Graphite Washed with Deionized Water and Ultrasonication (GU)

The impurity profile of the GU sample was similar to that of GW, with metal concentrations remaining at low levels. Nickel and manganese were measured at 0.060 mg g^{-1} and 0.020 mg g^{-1}, values comparable to those of GW. Cobalt remained the dominant impurity at 1.06 mg g^{-1}, essentially unchanged relative to water washing alone. Lithium was quantified at 0.44 mg g^{-1}, slightly higher than in GW but still more than two orders of magnitude lower than in the pristine black mass. The slightly higher Li signal may also reflect enhanced dispersion of fine particulates or surface-exposed salts due to ultrasonic agitation, which can increase accessibility of loosely bound ions [33–35]. Phosphorus, iron, copper and aluminum also remained below 0.2 mg g^{-1}. Consistently, the removal percentages in Table 1 show that GW and GU both achieve ≥99–100% removal of Ni, Mn, Al and Li and ≈98–99% removal of Co and Cu relative to BM. These results indicate that ultrasonication does not significantly change the average impurity concentration but may promote more uniform removal of loosely bound residues.

3.1.3. Graphite Washed with 0.1 M H_2SO_4 (GA)

The mild acid washing with 0.1 M sulfuric acid (GA) produced the most effective purification among all treatments. As shown in Table 1, nickel decreased to 0.037 mg g^{-1}, cobalt to 0.466 mg g^{-1} and lithium to 0.175 mg g^{-1}. Copper approached the detection limit at 0.019 mg g^{-1}, while manganese and aluminum were not detected. Iron and phosphorus persisted at 0.144 mg g^{-1} and 0.056 mg g^{-1}, respectively. Relative to BM, these values correspond to removal efficiencies of ≈99.9% for Ni, 99.3% for Co and 99.5% for Li, with Mn and Al reduced to below the detection limit and Cu by 99.6% (Table 1). These results show that diluted sulfuric acid dissolves residual metal oxides and current-collector fragments more efficiently than physical agitation alone, substantially reducing the metal burden of the graphite fraction [8,36,37]. The remaining trace cobalt and iron are likely associated with strongly bound surface complexes or chemically stable oxide or spinel-type residues [31].

Overall, the data demonstrate that the initial hydrometallurgical leaching step, followed by even simple water washing, already converts the mixed black mass into a graphite-rich fraction in which NMC-type metals are reduced by two to three orders of magnitude relative to BM [31]. Within this cleaned residue, the different post-leaching strategies then have distinct roles. The water-based treatments (GW and GU) efficiently

remove soluble salts, electrolyte residues and loosely bound particles, lowering Ni, Mn and Li into the sub-mg g^{-1} range but leaving measurable Co and trace levels of other metals associated with the graphite. Ultrasonication does not drastically change the average bulk impurity levels compared with simple water washing, which indicates that mechanical agitation alone is insufficient to detach the remaining strongly adhered or chemically stable species; rather, its main effect is to promote more uniform local cleaning and dispersion, as reflected by subtle improvements in SEM–EDX and Raman metrics. In contrast, the mild sulfuric-acid wash (GA) provides a clear additional purification step: bulk Ni, Co and Li are reduced to their minimum values, Mn and Al fall below the ICP-OES detection limit, and Co and Ni are at or below the practical SEM–EDX detection limit on graphite-rich particles. This behavior is consistent with the known ability of diluted H_2SO_4 to dissolve residual transition-metal oxides and current-collector fragments that are not fully removed by physical rinsing alone [31,37]. The combined ICP-OES and SEM–EDX trends therefore support the conclusion that, within an already leached industrial residue, mild acid washing is the most effective low-intensity route for further reducing the metal burden of the graphite-rich solid while preserving the carbon framework. However, even in the most purified fraction (GA), the residual Co concentration of ~0.47 mg g^{-1} (≈470 ppm) and comparable levels of other transition metals remain above the low-ppm impurity levels typically targeted for battery-grade materials [30]. This indicates that the washed graphite should be regarded as a thoroughly cleaned intermediate rather than a fully battery-grade product.

The residual transition-metal levels, particularly Co and Fe, are most likely associated with chemically stable surface complexes or spinel-type oxide phases that resist dissolution under the mild conditions applied here [8,36,37]. Achieving lower metal contents would therefore require either a higher acid concentration, an oxidizing agent such as H_2O_2 to promote dissolution of stable oxide phases, or an elevated temperature during the acid washing step, all of which would need to be balanced against the risk of introducing new contaminants or damaging the graphite structure. The persistent PVDF and separator-derived fluorinated residues, evidenced by XRD and DSC, represent a separate purification challenge that is not addressed by aqueous washing alone. Removal of these fluorinated species requires dedicated binder-extraction steps; a promising low-impact direction identified in ongoing work is the use of non-toxic or low-toxicity solvents under controlled temperature conditions, which could selectively dissolve PVDF without degrading the graphite framework and thereby reduce the remaining organic and fluorine burden prior to or following the hydrometallurgical washing steps described here [27].

3.2. X-Ray Diffraction (XRD) Analysis

The progressive purification of graphite recovered from spent NMC111 battery black mass was evaluated by X-ray diffraction (XRD), targeting the phase composition, impurity evolution, and structural order across four treatment stages: untreated black mass (BM), graphite washed with water (GW), graphite washed with water with ultrasonic pulses (GU), and graphite washed with acid (GA).

XRD analysis of the black mass (BM) reflects the complex mixture typical of spent Li-ion batteries, including intense reflections from the layered NMC111 cathode phase, metallic Fe and Ni, and graphitic carbon, as shown in Figure 2.

In the diffractogram of the graphite washed with water (GW), NMC-related and metallic peaks (Fe, Ni) are substantially reduced in intensity compared with BM, reflecting the dissolution and removal of water-soluble and weakly bound phases. Introducing ultrasonication (GU) does not lead to a dramatic further suppression of these reflections, but it slightly decreases the residual impurity peaks and marginally sharpens the graphite

(002) reflection, consistent with improved local cleaning and dispersion of the graphite-rich particles [38].

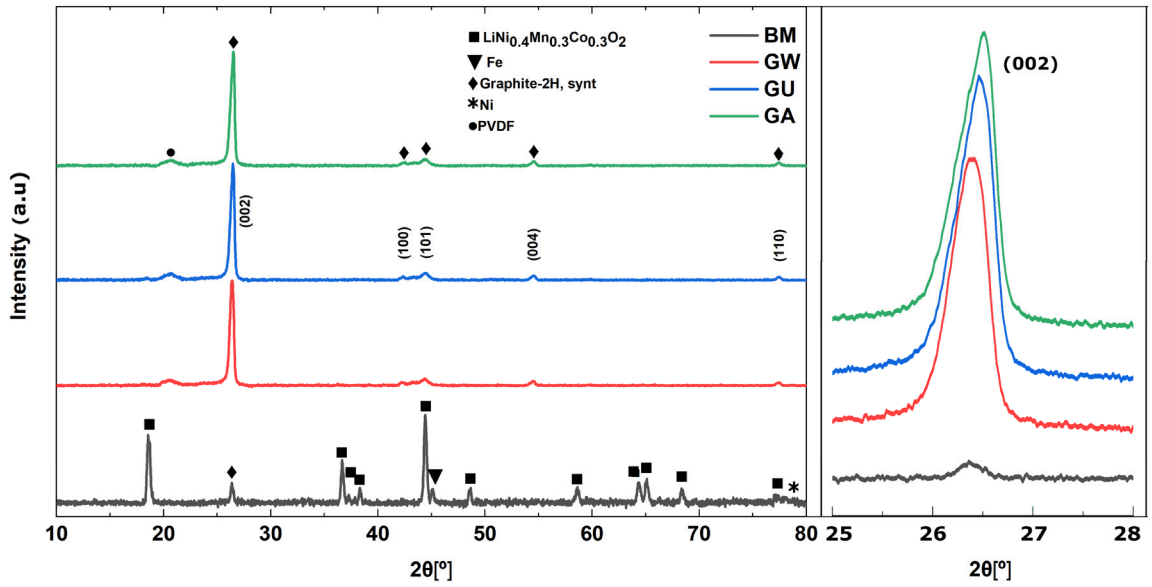

Figure 2. XRD diffractograms of black mass (BM) and washed graphite samples (GW, GU, and GA). Right panel: magnified view of the 25–28° 2θ range highlighting the graphite (002) reflection.

The (002) graphite peak shifted from 3.37705 Å (GW) to 3.36865 Å (GU) and finally to 3.3513 Å (GA), which signifies a sequential contraction of the interlayer spacing as residual intercalants are removed. These shifts and the progressive sharpening of the graphite (002) peak are clearly visible in the magnified 25–28° 2θ region shown in the right panel of Figure 2. The expansion of interplanar space in GW and GU is probably caused by trapped water, ions, or organics, consistent with reports on graphite intercalation and disorder [34]. Acid washing achieves nearly ideal spacing, indicating the best restoration of bulk graphite order [12,39–41]. Nevertheless, despite a marked purification, the characteristic PVDF reflection remains visible, indicating persistence of the binder, confirming its chemical resistance against dilute acid and mild physical processing [16,19].

A weak residual peak around 19° (2θ) is still discernible in the washed samples, which we attribute to remaining NMC-derived and/or polymer-rich phases that persist even after leaching and washing. In the starting BM, such low-intensity contributions are largely obscured by the much stronger NMC reflections, whereas in the washed samples they become visible once the dominant oxide phases are removed. At the same time, PVDF is not easily resolved in BM because its relatively weak and broadened reflections are overlapped by intense NMC and graphite peaks; after washing, when NMC-type reflections are suppressed, the PVDF-related feature becomes more apparent.

In summary, the XRD and complementary chemical data validate that the employed washing processes efficiently eliminate most transition-metal and oxide contaminants, unlock higher graphite crystallinity, and restore near-ideal lattice parameters.

3.3. Thermal Analysis

Thermogravimetric (TGA) and derivative thermogravimetric (DTG) curves of the washed graphite samples GW, GU and GA were recorded under synthetic air from 40 to 800 °C and are shown in Figure 3. All three samples exhibit a gradual mass loss from the start of the measurement, followed by a more pronounced oxidation event with a single DTG maximum at approximately 489 °C. This behavior is characteristic of the oxidative

combustion of graphite in air and is consistent with reports on recycled anode graphite from spent lithium-ion batteries, which typically show major mass loss in the 400–600 °C range under similar heating conditions. The main oxidation peak occurs at a considerably lower temperature than that of highly crystalline reference graphite, which generally oxidizes at ≥650–700 °C in air, reflecting the higher reactivity of recycled graphite associated with residual defects, smaller crystallite size and surface heterogeneities introduced during battery operation and processing [19,42,43].

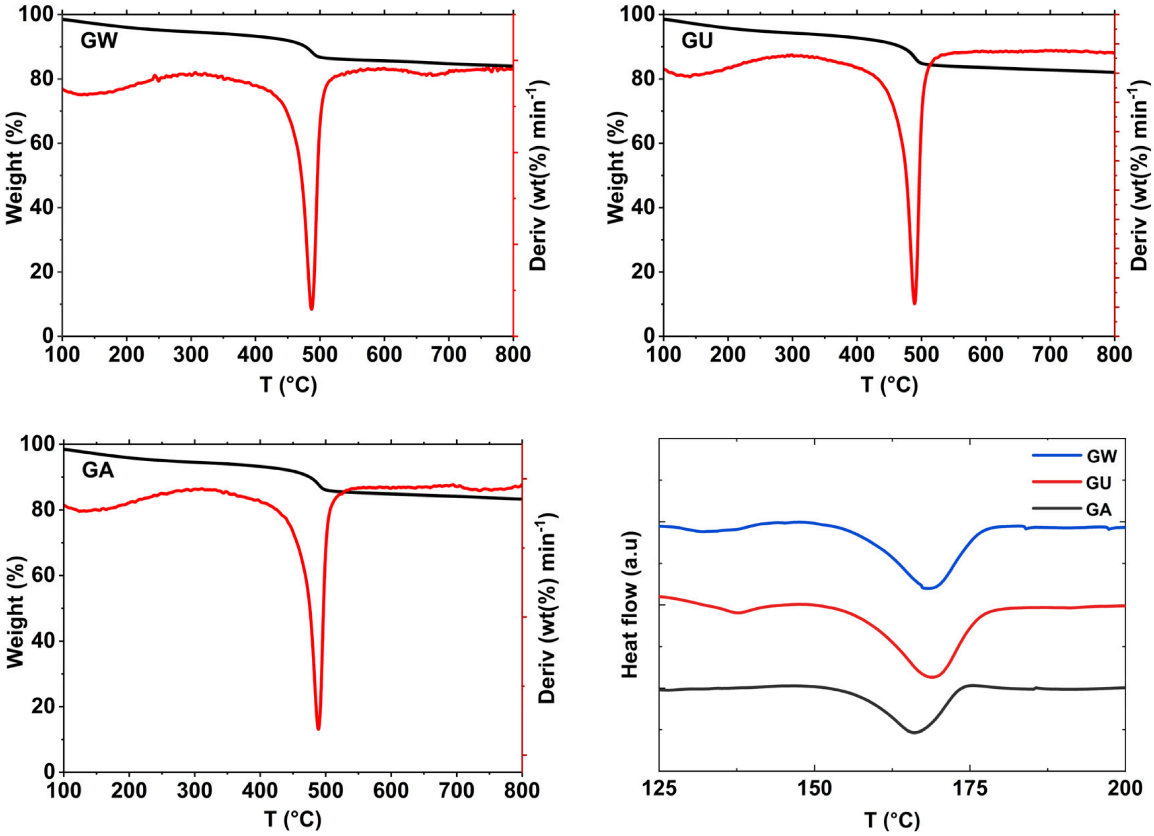

Figure 3. TGA (black) and DTG (red) curves of GW, GU and GA recorded under synthetic air (10 °C min^{-1}, 100–800 °C), showing the main oxidative combustion event with a DTG maximum near 489 °C and residual masses of ~82–84 wt% at 800 °C indicating incomplete combustion within the measurement range. DSC curves (bottom right, nitrogen atmosphere, 125–200 °C) display a 150–180 °C endotherm attributed to PVDF-binder residues, decreasing in the order GW > GU > GA.

The TGA curves show that oxidative combustion was not complete within the measurement range of 800 °C, with a residual mass of approximately 82–84 wt% remaining at the end of the run. The total mass loss between 40 and 800 °C was approximately 16 wt% for GW, 18 wt% for GU and 17 wt% for GA. These values represent a lower bound on the oxidizable carbon fraction under these conditions, as slow progressive oxidation of the graphite matrix continues beyond 800 °C. The incomplete combustion is consistent with the presence of PVDF coating and surface residues that partially protect the graphite from oxidation at lower temperatures, as independently confirmed by XRD and DSC. For this reason, the carbon content of the washed fractions is more reliably estimated from SEM–EDX analysis, which indicates approximately 82 wt% C for all three samples (Table 2), in good agreement with the graphite-dominated composition confirmed by XRD.

The slightly larger total mass loss in GU (~18 wt%) compared with GW (~16 wt%), and the marginally greater combustion contribution near 489 °C visible in the DTG curve of GU, are consistent with enhanced dispersion of graphite particles by ultrasonication,

which may expose a slightly greater reactive surface area to oxidation. Nevertheless, the overall oxidation profiles of GW, GU and GA are nearly overlapping, indicating that the different washing treatments do not markedly alter the intrinsic oxidative stability of the graphite. Instead, the washing steps primarily remove volatile and loosely bound species while leaving the bulk carbon structure essentially unchanged. This interpretation is supported by the low and similar high-temperature residues for all three samples and by ICP-OES analysis, which shows that Co, Ni, Mn and Al are reduced to trace levels after washing, far below the graphite content and insufficient to dominate the oxidation behavior [16,23,44–47].

Taken together, the TGA–DTG data support the conclusion that the post-leaching washing steps clean the material without degrading the underlying graphite framework.

Differential scanning calorimetry (DSC) curves for the three samples (Figure 3) show a single endothermic event between 150 and 180 °C, with the peak depth clearly decreasing in the order GW > GU > GA. This temperature interval coincides with the reported melting range of semi-crystalline PVDF binders used in Li-ion electrodes (typically 160–175 °C) and is therefore consistent with residual PVDF-based binder and/or electrolyte-derived organic species in the recovered graphite [27,48]. The systematic reduction in peak intensity from GW to GA indicates a progressive decrease in the amount of such organic residues as the washing treatments become more aggressive, in agreement with the diminished low-temperature mass loss observed in TGA and with the literature showing that regeneration processes reduce binder and electrolyte remnants on spent graphite surfaces [19,27].

In the temperature range between ~100 and 350 °C, both the DTG and DSC curves display features that partially overlap in this region, and it is important to clarify their physical origin. In the DTG curves recorded under synthetic air, a broad low-amplitude signal is visible in this interval, most prominently in GW, which corresponds to a small but continuous mass loss of approximately 1–2 wt% attributed to the volatilization of residual low-boiling organic species including electrolyte-derived compounds and surface-adsorbed organics that remain on the graphite after washing. In parallel, the DSC curves recorded under nitrogen show a single well-defined endothermic event with a peak minimum near 163–168 °C, which we assign to the melting of semicrystalline PVDF binder residues present on the graphite surface, consistent with the reported melting range of PVDF used in lithium-ion electrode formulations (155–175 °C). The apparent overlap between the DTG and DSC signals in this temperature window is therefore physically expected and mutually consistent; the DSC captures the solid-to-melt phase transition of PVDF under inert conditions, while the DTG reflects the concurrent volatilization of co-existing low-boiling organic species under oxidative conditions. These are complementary responses of the same heterogeneous organic surface layer to thermal treatment, not competing or contradictory events. The progressive decrease in both signals in the order GW > GU > GA provides coherent evidence that the mild acid wash most effectively reduces the combined burden of PVDF and volatile organic residues on the graphite surface.

3.4. Scanning Electron Microscopy and Energy Dispersive X-Ray Spectrometry (SEM–EDX) Analysis

The SEM–EDX analysis was carried out on the solid residues obtained after leaching of the black mass and subsequent washing steps, namely GW, GU, and GA, with the untreated black mass BM included for comparison. Figure 4 shows representative SEM micrographs and their associated EDX spectra.

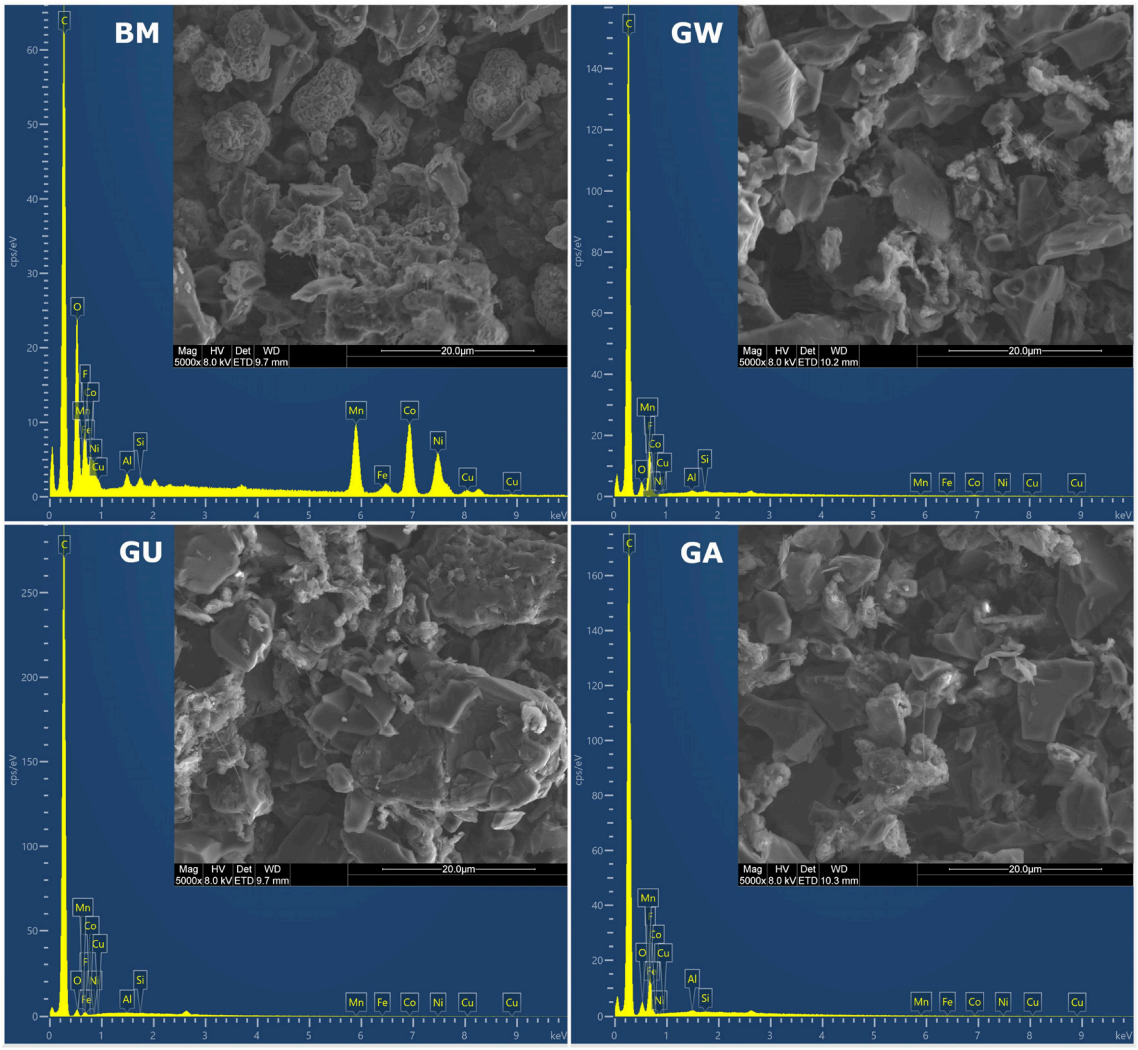

Figure 4. Scanning electron microscopy images (SEM) and elemental analysis (EDX) of black mass (BM) and washed graphite samples (GW, GU and GA).

The corresponding EDX quantitative data are summarized in Table 2. Values are reported as mean plus or minus one standard deviation based on several particle measurements, which reflects both measurement uncertainty and real local variation at the micrometer scale. For elements with mean values clearly above about 0.1 wt%, this mean plus or minus standard deviation gives a reasonable estimate of the local composition of the carbon-rich particles, whereas for elements with mean values below about 0.1 wt%, the values lie at or below the practical detection limit of EDX and are therefore best described qualitatively as trace signals.

At high SEM magnification, the as-received BM reveals a densely packed and strongly agglomerated powder composed of large cauliflower-like aggregates and irregular plate-like fragments decorated with fine submicrometric debris. This heterogeneous morphology is typical of spent NMC111 battery-type black mass [38], in which cathode fragments, carbonaceous material, binder, and current collector debris remain intimately mixed and attached to one another. The corresponding EDX spectrum and the mean composition in Table 2 show C and O together with more than 20 wt% combined Ni, Co and Mn, about 6 wt% F and several other elements such as Al, Fe, Cu, Zn, Ca, Si and P, consistent with a mixture of NMC-type oxide, metallic phases and electrolyte or binder residues in the analyzed regions. These observations agree with the high bulk metal contents

obtained by ICP-OES for BM and confirm that the starting black mass is metal-rich and strongly heterogeneous.

After leaching and simple water washing (GW), SEM images reveal mainly angular plate-like particles with comparatively smooth facets and fractured flake edges, arranged in compact agglomerates. The cauliflower-type aggregates seen in BM are largely absent, and the number of fine debris attached to particle surfaces appears reduced, indicating that leaching and rinsing have removed a significant part of loosely bound inorganic and metal-rich material. Thin filament-like features are occasionally observed, which may correspond to polymer or separator fragments, but their exact nature cannot be determined at this magnification. The associated EDX spectrum is dominated by C, and the mean composition in Table 2 indicates an increase in C to about 82 wt%, a decrease in O to about 5 wt% and a strong reduction in Ni, Co and Mn to 0.09, 0.23 and 0.02 wt%, respectively. These metal levels are more than an order of magnitude lower than in BM and indicate that the plate-like particles are strongly depleted in NMC-type phases.

Introducing ultrasonic agitation (GU) further disrupts the agglomerates; SEM reveals large, compact agglomerates of plate-like particles with relatively smooth, faceted surfaces and rounded edges. Compared with GW, some particle surfaces appear cleaner, with fewer fine particulates attached, while other regions show strongly consolidated aggregates, which is consistent with sonication both disrupting and rearranging particle contacts. Thin fibrous fragments are also occasionally observed. The GU EDX spectrum and mean values in Table 2 are very similar to those of GW, with about 82 wt% C, 5–6 wt% O, and 12 wt% F. Ni, Co, and Mn are 0.07, 0.19, and 0.02 wt%, respectively, which, within the standard deviations, are only slightly lower than in GW and still close to the EDX detection limit. This behavior agrees with ICP-OES, which shows that ultrasonication does not markedly change the average bulk concentrations of transition metals, suggesting that its main effect is to improve local cleaning and dispersion rather than to remove a large additional amount of metal impurities.

With the dilute H_2SO_4 wash (GA), SEM shows aggregates of angular, plate-like particles with relatively smooth, well-defined facets and fewer obvious dense inclusions than in the other samples. Many plates appear cleaner, although patches of finer, irregular material and occasional fibrous fragments remain attached to some surfaces, indicating that the acid treatment substantially reduces but does not eliminate non-carbonaceous residues on the graphite-rich particles. The GA EDX spectrum is strongly dominated by C, and the mean composition in Table 2 remains at about 82 wt% C, 6 wt% O and 12 wt% F, while Ni, Co and Mn fall to 0.01, 0.07 and 0.01 wt%. These metal values are at or below the typical detection limit for EDX under standard conditions (about 0.1 wt% for most elements), so they should be interpreted as, at most, trace levels with high relative uncertainty rather than precise quantitative concentrations. The approximately constant F content across GW, GU and GA supports the XRD observation that PVDF-related reflections persist after all washing steps and indicates that fluorinated binder- and electrolyte-derived species are only partly removed. The higher F wt% in the washed samples (~12 wt%) compared with BM (6.3 wt%) does not imply true fluorine enrichment, but reflects the way EDX normalizes surface compositions: in BM, the graphite surfaces also carry substantial amounts of Ni, Co, Mn and other metals, so F is diluted in the wt% balance, whereas after washing, these heavy elements are largely removed and C increases from ~49 wt% to ~82 wt%, so a similar absolute F signal appears as a larger relative fraction. In other words, the EDX data indicate that PVDF-derived species remain present on the graphite-rich particles after washing, but they do not show an increase in the absolute fluorine inventory of the material.

In the washed fractions GW, GU and GA, the largest plate-like particles observed by SEM are therefore consistent with graphite-rich grains, because XRD shows graphite as the

dominant crystalline phase and the NMC and metal reflections are strongly suppressed, while EDX on these regions reveals high local carbon contents with only minor amounts of heteroatoms [46,47]. At the same time, patches of attached irregular material and the residual signals of F, O and trace metals demonstrate that these graphite-rich particles display different degrees of surface cleanliness rather than completely pristine graphite surfaces [48].

When the EDX results are compared with the ICP-OES measurements, a coherent picture emerges. Starting from BM and ordered according to the processing steps, GW, GU, and GA, all the cleaning techniques show the same monotonic decrease in Ni, Co, and Mn, even though the absolute concentrations differ due to their different sampling volumes and detection limits. ICP-OES provides bulk elemental concentrations after complete digestion of the powder and has detection limits in the range of 10^{-9} to 10^{-6} wt%, several orders of magnitude lower than EDX. The ICP-OES data confirm that Ni, Co and Mn in the GA graphite fraction are below 0.02 wt%. In contrast, EDX shows that, within its detection limit, the particles examined in the microscope are strongly enriched in carbon-containing phases and display transition-metal signals only at trace levels or are not detectable at all [28,49]. Together with the XRD evidence for the strong suppression of NMC type and metallic reflections, these complementary observations support the conclusion that the post-leaching washing sequence, and in particular the mild acid treatment, leads to a graphite-rich fraction in which transition-metal-bearing crystalline phases are largely removed, while a fluorine-containing carbon surface, attributed to PVDF and electrolyte residues, remains [16,45,47,48,50].

3.5. Raman Spectroscopy Analysis

Raman spectroscopy was used to evaluate the structural order of the carbon fraction recovered from spent NMC111 black mass. The spectra in Figure 5 show the characteristic D band (≈1350 cm^{-1}), G band (≈1580 cm^{-1}) and G′ (2D) band (≈2700 cm^{-1}), which are the main features of sp^2-bonded, graphite-like carbon. The D band arises from defect-activated breathing modes of sp^2 carbon rings, the G band from in-plane C–C stretching vibrations, and the G′ band is the second-order overtone associated with the D band; their positions, widths and relative intensities provide information on defect density, crystallite size and stacking order in graphitic materials [49]. To minimize the influence of separator fibers and other non-graphitic residues that are still present in the washed fractions, the spectra analyzed here were collected on regions where the graphite-related bands dominated the signal, as identified in the SEM images.

The main Raman parameters extracted from the spectra of GW, GU and GA are summarized in Table 3.

The I_D/I_G ratio decreases strongly with the washing sequence, from 0.62 for GW to 0.52 for GU and 0.11 for GA, indicating a significant reduction in defect density [16,21,51]. It should be noted that these ratios were determined from the integrated peak areas of the D and G bands obtained by peak fitting, rather than from peak heights [52,53]. For GW, which exhibits the highest defect density among the three fractions, the D band is substantially broader than the G band; consequently, the area-based I_D/I_G ratio of GW (0.62) is consistent with the spectra shown in Figure 5. This behavior is physically expected for Stage 1 disordered graphitic carbon [52]. For GU and GA, as structural order improves, the D band narrows and the area- and height-based ratios converge, consistent with their visual appearance in Figure 5.

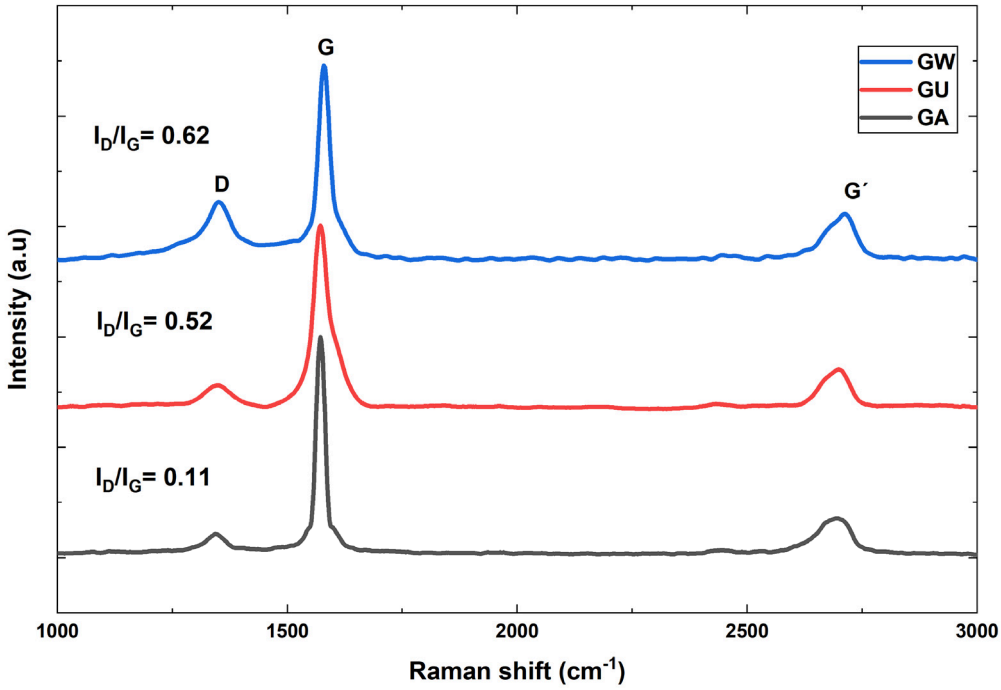

Figure 5. Raman spectra of graphite recovered from spent NMC111 black mass after different washing treatments (GW, GU, GA), showing the D, G and G′ bands and the corresponding I_D/I_G ratios used to assess defect density and structural ordering.

For 532 nm excitation, the in-plane crystallite size La was estimated using the empirical relation La (nm) = C(λ)/(I_D/I_G), with C(532 nm) ≈ 19 nm, following Cançado et al. and related work on nanographite under visible excitation [54]. Using this inverse relation between I_D/I_G and La, the corresponding La values increase from 30.6 nm (GW) to 36.6 nm (GU) and 168.4 nm (GA), confirming the development of more extended ordered sp^2 domains after washing [53].

The small downshifts in the D and G bands (from 1351 to 1345 cm^{-1} and from 1580 to 1572 cm^{-1}, respectively) are consistent with a partial relaxation of compressive strain and a reduction in heteroatom-induced perturbations in the carbon network as surface contaminants and intercalated species are removed. In parallel, the G′ band shifts from 2752 to 2696 cm^{-1} and remains well-defined, which is characteristic of an increase in stacking order and a transition from more turbostratic arrangements towards better ordered multilayer graphite, as reported for purified or thermally treated graphite-based materials [55,56].

These Raman trends are coherent with the complementary characterization. The increase in L_a and the reduction in I_D/I_G correlate with XRD patterns in which graphite reflections become dominant, and NMC-related or metal-bearing phases are markedly reduced after washing, especially for GA, and with a contraction of the d002 spacing towards values typical of well-ordered graphite [53]. The progressive decrease in defect-related Raman intensity also agrees with EDX and ICP-OES results, which show a strong reduction in Ni, Co and Mn contents and only trace metal signals on the graphite-rich particles in GA, and with DSC, which indicates a reduction in inorganic and binder fractions. Taken together, these observations show that the washing and mild acid treatment not only remove residual active material and binder species but are also associated with a substantial improvement in the structural ordering of the recovered graphite, making it a suitable precursor for further value adding treatments such as expansion, exfoliation or conversion into high-surface-area adsorbents, thereby enhancing its added value within circular battery-material workflows [25,46].

4. Conclusions

This study shows that graphite can be efficiently cleaned and structurally preserved from industrial NMC111 black mass by using simple hydrometallurgical washing steps carried out under mild conditions. The initial leaching with 2 M H_2SO_4 and 3% H_2O_2 is responsible for most of the removal of NMC metals derived from the mixed black mass, but it does not by itself produce a clean graphite product. The additional water-based and diluted H_2SO_4 washing steps are therefore important because they remove the remaining metal-bearing surface phases, salts and fine oxide or spinel fragments that are not fully detached during leaching.

Bulk ICP-OES and surface-sensitive SEM–EDX measurements show that, within the leached residue, water washing and water plus ultrasonication already reduce Ni, Co, Mn and Li by two to three orders of magnitude compared with the starting material, although small amounts of Co and other metals are still associated with the graphite. The mild sulfuric acid wash (GA) provides an additional improvement: it produces the lowest residual metal contents, with several transition metals at or below the detection limits and only trace signals observed on graphite-rich particles. XRD, TGA/DSC and Raman analysis confirm that this acid-washed fraction maintains a coherent graphite framework, shows a contraction of the d_{002} spacing and larger in-plane crystallite sizes, and contains only modest amounts of PVDF and separator-derived residues. For this reason, it is most accurately described as a thoroughly cleaned low-metal graphite fraction rather than an entirely impurity-free material. The remaining transition-metal levels are still higher than standard battery-grade specifications, so additional purification or regeneration would be required for use in high-performance anodes.

The properties of this fraction bring it significantly closer to the impurity levels and structural quality required for secondary applications and for subsequent, lower intensity regeneration or surface modification treatments. This can, in turn, reduce the need for very energy-intensive high-temperature steps or strongly oxidizing conditions in later stages of the recycling chain. By quantifying both the benefits and the limitations of three simple post-leaching washing options applied to a real industrial residue, this study offers practical guidance for designing low-impact graphite cleaning steps that can be integrated into existing hydrometallurgical battery recycling flowsheets.

Author Contributions: Conceptualization, J.E.A.-F. and M.P.; methodology, J.E.A.-F., and M.P.; software, J.E.A.-F.; validation, J.E.A.-F., M.L., M.Z., E.K. and M.P.; formal analysis, J.E.A.-F.; investigation, J.E.A.-F., M.P., M.Z., M.L. and E.K.; resources, M.P., S.Ö.; data curation, J.E.A.-F.; writing—original draft preparation, J.E.A.-F.; writing—review and editing, J.E.A.-F., M.L., M.Z., E.K. and M.P.; visualization, J.E.A.-F., M.P., and J.L.; supervision, M.P.; project administration, S.Ö. funding acquisition, M.P. All authors have read and agreed to the published version of the manuscript.

Funding: This research was primarily funded by the Swedish Energy Agency (P2023-00146), via the programme Batterifonden, together with participating industrial partners Grafren AB and 2D fab AB.

Data Availability Statement: The original contributions presented in this study are included in the article. Further inquiries can be directed to the corresponding author.

Acknowledgments: The authors gratefully acknowledge financial support from the Swedish Energy Agency. The authors also thank the Chalmers Materials Analysis Laboratory (CMAL) for providing access to and support with materials characterization.

Conflicts of Interest: Author Magnus Larsson was employed by the company 2D fab AB. Authors Sofia Öiseth and Jonas Löfvendahl were employed by the company Chalmers Industriteknik. Authors Mykhailo Zhybak and Erik Khranovskyy were employed by the company GRAFREN. The remaining authors declare that the research was conducted in the absence of any commercial or financial relationships that could be construed as a potential conflict of interest.

References

1. Nair, A.V.; Jayasree, S.S.; Baji, D.S.; Nair, S.; Santhanagopalan, D. Environment-friendly acids for leaching transition metals from spent-NMC532 cathode and sustainable conversion to potential anodes. *RSC Sustain.* **2024**, *2*, 2377–2388. [CrossRef]
2. European Commission. *Critical Raw Materials Resilience: Charting a Path Towards Greater Security and Sustainability*; European Commission: Brussels, Belgium, 2020. Available online: https://ec.europa.eu/docsroom/documents/42849 (accessed on 25 May 2026).
3. Natarajan, S.; Divya, M.L.; Aravindan, V. Should we recycle the graphite from spent lithium-ion batteries? The untold story of graphite with the importance of recycling. *J. Energy Chem.* **2022**, *71*, 351–369. [CrossRef]
4. Or, T.; Gourley, S.W.D.; Kaliyappan, K.; Yu, A.; Chen, Z. Recycling ofmixed cathode lithium-ion batteries for electric vehicles: Current status and future outlook. *Carbon Energy* **2020**, *2*, 6–43. [CrossRef]
5. Jara, A.D.; Betemariam, A.; Woldetinsae, G.; Kim, J.Y. Purification, application and current market trend of natural graphite: A review. *Int. J. Min. Sci. Technol.* **2019**, *29*, 671–689. [CrossRef]
6. Jena, K.K.; AlFantazi, A.; Mayyas, A.T. Comprehensive Review on Concept and Recycling Evolution of Lithium-Ion Batteries (LIBs). *Energy Fuels* **2021**, *35*, 18257–18284. [CrossRef]
7. Harper, G.; Sommerville, R.; Kendrick, E.; Driscoll, L.; Slater, P.; Stolkin, R.; Walton, A.; Christensen, P.; Heidrich, O.; Lambert, S.; et al. Recycling lithium-ion batteries from electric vehicles. *Nature* **2019**, *575*, 75–86. [CrossRef]
8. Chen, Q.; Huang, L.; Liu, J.; Luo, Y.; Chen, Y. A new approach to regenerate high-performance graphite from spent lithium-ion batteries. *Carbon* **2022**, *189*, 293–304. [CrossRef]
9. Srivastava, V.; Rantala, V.; Mehdipour, P.; Kauppinen, T.; Tuomikoski, S.; Heponiemi, A.; Runtti, H.; Tynjälä, P.; Simões Dos Reis, G.; Lassi, U. A comprehensive review of the reclamation of resources from spent lithium-ion batteries. *Chem. Eng. J.* **2023**, *474*, 145822. [CrossRef]
10. Rouquette, L.M.J.; Altenschmidt, L.; Culina, M.; Brant, W.R.; Ebin, B.; Petranikova, M. Kinetics study of the dissolution of black mass material using oxalic acid as a leaching agent. *J. Hazard. Mater. Adv.* **2025**, *18*, 100750. [CrossRef]
11. Gao, Y.; Zhang, S.; Lin, S.; Li, Z.; Chen, Y.; Wang, C. Opportunity and challenges in recovering and functionalizing anode graphite from spent lithium-ion batteries: A review. *Environ. Res.* **2024**, *247*, 118216. [CrossRef]
12. Abdollahifar, M.; Doose, S.; Cavers, H.; Kwade, A. Graphite Recycling from End-of-Life Lithium-Ion Batteries: Processes and Applications. *Adv. Mater. Technol.* **2022**, *8*, 2200368. [CrossRef]
13. Gao, S.-j.; Liu, W.-f.; Fu, D.-j.; Liu, X.-g. Research progress on recovering the components of spent Li-ion batteries. *New Carbon Mater.* **2022**, *37*, 435–460. [CrossRef]
14. Gorman, S.; Hitt, C.; Kesler, S.; Keoleian, G.; Kim, H.C.; De Kleine, R.; Anderson, J.E. US graphite sourcing for electric vehicle battery applications. *J. Ind. Ecol.* **2025**, *29*, 2162–2181. [CrossRef]
15. Lai, Y.; Zhu, X.; Li, J.; Gou, Q.; Li, M.; Xia, A.; Huang, Y.; Zhu, X.; Liao, Q. Recovery and regeneration of anode graphite from spent lithium-ion batteries through deep eutectic solvent treatment: Structural characteristics, electrochemical performance and regeneration mechanism. *Chem. Eng. J.* **2023**, *457*, 141196. [CrossRef]
16. Wang, H.; Huang, Y.; Huang, C.; Wang, X.; Wang, K.; Chen, H.; Liu, S.; Wu, Y.; Xu, K.; Li, W. Reclaiming graphite from spent lithium ion batteries ecologically and economically. *Electrochim. Acta* **2019**, *313*, 423–431. [CrossRef]
17. Nazari, P.; Hamidi, A.; Golmohammadzadeh, R.; Rashchi, F.; Vahidi, E. Upcycling spent graphite in LIBs into battery-grade graphene: Managing the produced waste and environmental impacts analysis. *Waste Manag.* **2024**, *174*, 140–152. [CrossRef]
18. Maeng, S.; Ha, J.; Lee, J.; Kim, Y.-T.; Choi, J. Upcycling of spent graphite and iron housing from waste lithium-ion batteries for fabricating cost-effective high-capacity anodes. *Green Chem.* **2023**, *25*, 9981–9992. [CrossRef]
19. Dziejarski, B.; Arevalo Fester, J.E.; Serafin, J.; Petranikova, M.; Tam, E.; Martinelli, A.; Krzyżyńska, R.; Andersson, K.; Knutsson, P. Valorization of hazardous graphite from black mass (NMC 111) of lithium-ion battery recycling via KOH activation for functional carbon design. *Mater. Des.* **2025**, *254*, 114073. [CrossRef]
20. Li, P.; Liu, Q.; Møller, M.; Wang, D.; Jensen, L.R.; Xia, X. Direct regeneration of spent lithium-ion batteries: A mini-review. *Mater. Lett.* **2024**, *357*, 135724. [CrossRef]
21. Yu, H.; Chen, X.; Zhou, J.; Wang, H.; Qiu, S. Premium defect-enriched graphite from spent anodes of lithium ion batteries. *J. Alloys Compd.* **2023**, *960*, 170876. [CrossRef]
22. Milian, Y.E.; Jamett, N.; Cruz, C.; Herrera-Leon, S.; Chacana-Olivares, J. A comprehensive review of emerging technologies for recycling spent lithium-ion batteries. *Sci. Total Environ.* **2024**, *910*, 168543. [CrossRef]
23. Mancini, M.; Hoffmann, M.F.; Martin, J.; Weirather-Köstner, D.; Axmann, P.; Wohlfahrt-Mehrens, M. A proof-of-concept of direct recycling of anode and cathode active materials: From spent batteries to performance in new Li-ion cells. *J. Power Sources* **2024**, *595*, 233997. [CrossRef]
24. Sahivirta, H.; Wilson, B.P.; Lundstrom, M.; Serna-Guerrero, R. A study on recovery strategies of graphite from mixed lithium-ion battery chemistries using froth flotation. *Waste Manag.* **2024**, *180*, 96–105. [CrossRef] [PubMed]

25. Zhang, J.; Li, J.; Wang, Y.; Sun, M.; Wang, L.; Tu, Y. Separation of Graphites and Cathode Materials from Spent Lithium-Ion Batteries Using Roasting–Froth Flotation. *Sustainability* **2022**, *15*, 30. [CrossRef]
26. Vieceli, N.; Benjamasutin, P.; Promphan, R.; Hellström, P.; Paulsson, M.; Petranikova, M. Recycling of Lithium-Ion Batteries: Effect of Hydrogen Peroxide and a Dosing Method on the Leaching of LCO, NMC Oxides, and Industrial Black Mass. *ACS Sustain. Chem. Eng.* **2023**, *11*, 9662–9673. [CrossRef]
27. Akbaş, Y.; Petranikova, M.; Ebin, B. Co-solvent controlled PVDF extraction from spent Li-ion batteries using supercritical CO_2. *Sep. Purif. Technol.* **2025**, *376*, 134056. [CrossRef]
28. Wang, X.; Zhou, J.; Wang, H.; Zhang, J.; Ma, X.; Qiu, S.; Chen, L. Mildly expanded graphite with exceptional performance from waste lithium ion batteries by space-confined intercalation of deep eutectic solvent. *Sep. Purif. Technol.* **2025**, *354*, 129329. [CrossRef]
29. Xie, X.; Fan, W.; Zhang, J.; Ma, R.; Chen, Y.; Wang, C. Regeneration of graphite anode from spent lithium iron phosphate batteries: Microstructure and morphology evolution at different thermal-repair temperature. *Powder Technol.* **2023**, *430*, 118998. [CrossRef]
30. Li, M.; Mo, R.; Ding, A.; Zhang, K.; Guo, F.; Xiao, C. Electrochemical technology to drive spent lithium-ion batteries (LIBs) recycling: Recent progress, and prospects. *Energy Mater.* **2024**, *4*, 400070. [CrossRef]
31. Yang, Y.; Song, S.; Lei, S.; Sun, W.; Hou, H.; Jiang, F.; Ji, X.; Zhao, W.; Hu, Y. A process for combination of recycling lithium and regenerating graphite from spent lithium-ion battery. *Waste Manag.* **2019**, *85*, 529–537. [CrossRef] [PubMed]
32. Li, R.; Zeng, S.; Wang, L.; Yu, X.; Zeng, H.; Liu, W.; Fu, D.; Liu, X. A facile approach for regeneration of graphite anodes from spent lithium-ion battery. *J. Alloys Compd.* **2024**, *993*, 174691. [CrossRef]
33. Jiang, F.; Chen, Y.; Ju, S.; Zhu, Q.; Zhang, L.; Peng, J.; Wang, X.; Miller, J.D. Ultrasound-assisted leaching of cobalt and lithium from spent lithium-ion batteries. *Ultrason. Sonochem.* **2018**, *48*, 88–95. [CrossRef]
34. Deng, H.; Hong, R.; Wang, B.; Xu, J.; Yang, G.; Shi, Z.; He, W.; Li, G. Ultrasonic enhanced preferential leaching process of Li from waste lithium-ion batteries using oxalic acid focused on optimization and mechanism. *Sep. Purif. Technol.* **2025**, *364*, 132327. [CrossRef]
35. Nguyen, V.S.; Rouxel, D.; Hadji, R.; Vincent, B.; Fort, Y. Effect of ultrasonication and dispersion stability on the cluster size of alumina nanoscale particles in aqueous solutions. *Ultrason. Sonochem.* **2011**, *18*, 382–388. [CrossRef]
36. Gao, Y.; Zhang, J.; Jin, H.; Liang, G.; Ma, L.; Chen, Y.; Wang, C. Regenerating spent graphite from scrapped lithium-ion battery by high-temperature treatment. *Carbon* **2022**, *189*, 493–502. [CrossRef]
37. Chen, W.-S.; Ho, H.-J. Recovery of Valuable Metals from Lithium-Ion Batteries NMC Cathode Waste Materials by Hydrometallurgical Methods. *Metals* **2018**, *8*, 321. [CrossRef]
38. Chernyaev, A.; Kobets, A.; Liivand, K.; Tesfaye, F.; Hannula, P.-M.; Kallio, T.; Hupa, L.; Lundström, M. Graphite recovery from waste Li-ion battery black mass for direct re-use. *Miner. Eng.* **2024**, *208*, 108587. [CrossRef]
39. Yi, C.; Zhou, L.; Wu, X.; Sun, W.; Yi, L.; Yang, Y. Technology for recycling and regenerating graphite from spent lithium-ion batteries. *Chin. J. Chem. Eng.* **2021**, *39*, 37–50. [CrossRef]
40. Yu, H.; Dai, H.; Zhu, Y.; Hu, H.; Zhao, R.; Wu, B.; Chen, D. Mechanistic insights into the lattice reconfiguration of the anode graphite recycled from spent high-power lithium-ion batteries. *J. Power Sources* **2021**, *481*, 229159. [CrossRef]
41. Dong, Y.; Zeng, Z.; Yuan, Z.; Wang, B.; Lei, H.; Zhao, W.; Ai, W.; Kong, L.; Yang, Y.; Ge, P. Spent graphite regeneration: Exploring diverse repairing manners with impurities-catalyzing effect towards high performance and low energy consumption. *J. Energy Chem.* **2024**, *91*, 656–669. [CrossRef]
42. Lu, Y.; Zhang, Z.; Zhong, Q.; Yao, Z.; Wu, J.; Zhang, J.; Wang, L.; Xiao, J. Oxygen-rich modified-graphite recycled from spent lithium batteries for improved lithium-ion storage: Adsorption and intercalation mechanisms. *Sep. Purif. Technol.* **2025**, *359*, 130798. [CrossRef]
43. Geng, Z.; Liu, J.; Geng, Y.; Peng, M.; Xiong, M.; Shi, H.; Luo, X. Separation and recovery of graphite from spent lithium–ion batteries for synthesizing micro-expanded sorbents. *New J. Chem.* **2022**, *46*, 20250–20259. [CrossRef]
44. Zhang, R.; Tian, Y.; Zhang, W.-l.; Song, J.-y.; Min, J.; Pang, B.; Chen, J.-j. Electrochemical methods for the removal of impurities from thegraphite anode in spent ternary lithium-ion batteries. *New Carbon Mater.* **2024**, *39*, 573–582. [CrossRef]
45. Cheng, Q.; Marchetti, B.; Chen, X.; Xu, S.; Zhou, X.-D. Separation, purification, regeneration and utilization of graphite recovered from spent lithium-ion batteries—A review. *J. Environ. Chem. Eng.* **2022**, *10*, 107312. [CrossRef]
46. Yuwen, C.; Liu, B.; Zhang, H.; Tian, S.; Zhang, L.; Guo, S.; Zhou, B. Efficient recovery and regeneration of waste graphite through microwave stripping from spent batteries anode for high-performance lithium-ion batteries. *J. Clean. Prod.* **2022**, *333*, 130197. [CrossRef]
47. Gomez-Moreno, L.A.; Klemettinen, A.; Serna-Guerrero, R. A simple methodology for the quantification of graphite in end-of-life lithium-ion batteries using thermogravimetric analysis. *iScience* **2023**, *26*, 107782. [CrossRef]
48. Haridass, R.; Sabu, A.; Augustin, N.; Annamalai, P.K.; Brahmadesam Thoopul Srinivasa Raghava, R. Effect of Polyvinylpyrrolidone on the Structure Development, Electrical, Thermal, and Wetting Properties of Polyvinylidene Fluoride-Expanded Graphite Nanocomposites. *ACS Omega* **2024**, *9*, 178–195. [CrossRef]

49. Zhang, W.; Liu, Z.; Xia, J.; Li, F.; He, W.; Li, G.; Huang, J. Preparing graphene from anode graphite of spent lithium-ion batteries. *Front. Environ. Sci. Eng.* **2017**, *11*, 6. [CrossRef]
50. Guyett, P.C.; Chew, D.; Azevedo, V.; Blennerhassett, L.C.; Rosca, C.; Tomlinson, E. Optimizing SEM-EDX for fast, high-quality and non-destructive elemental analysis of glass. *J. Anal. At. Spectrom.* **2024**, *39*, 2565–2579. [CrossRef]
51. Newbury, D.E.; Ritchie, N.W.M.; Mengason, M.; Scott, K. SEM/EDS Trace Analysis: Limits Imposed by Fluorescence of the Detector. *Microsc. Microanal.* **2017**, *23*, 1026–1027. [CrossRef]
52. Ferrari, A.C. Raman spectroscopy of graphene and graphite: Disorder, electron–phonon coupling, doping and nonadiabatic effects. *Solid State Commun.* **2007**, *143*, 47–57. [CrossRef]
53. Reich, S.; Thomsen, C. Raman spectroscopy of graphite. *Phil. Trans. R. Soc. Lond. A* **2004**, *362*, 2271–2288. [CrossRef]
54. Cançado, L.G.; Takai, K.; Enoki, T.; Endo, M.; Kim, Y.A.; Mizusaki, H.; Speziali, N.L.; Jorio, A.; Pimenta, M.A. Measuring the degree of stacking order in graphite by Raman spectroscopy. *Carbon* **2008**, *46*, 272–275. [CrossRef]
55. Hou, Y.; Guo, H.; Xing, B.; Zeng, H.; Kang, W.; Qu, X.; Zhang, C.; Jia, J.; Huang, G.; Cao, Y. Purification of spent graphite and surface modification with amorphous carbons as anodes for high-performance lithium-ion batteries. *Fuel* **2024**, *374*, 132488. [CrossRef]
56. Li, Y.; Lv, W.; Zhao, H.; Xie, Y.; Ruan, D.; Sun, Z. Regeneration of anode materials from complex graphite residue in spent lithium-ion battery recycling process. *Green Chem.* **2022**, *24*, 9315–9328. [CrossRef]